

Integration of UWB Radar on Mobile Robots for Continuous Obstacle and Environment Mapping

ADELINA GIUREA¹, STIJN LUCHIE¹, DIETER COPPENS¹, JEROEN HOEBEKE¹, ELI DE POORTER¹

¹Department of Information Technology, Ghent University - imec - IDLab, Technologiepark 126, 9052 Ghent, Belgium

Corresponding author: Adelina Giurea (e-mail: adelina.giurea@ugent.be)

The research that led to these results was partly funded by the DistriMuSe project (HORIZON-KDT-JU-2023-2-RIA) with Grant No 101139769

ABSTRACT This paper presents an infrastructure-free approach for obstacle detection and environmental mapping using ultra-wideband (UWB) radar mounted on a mobile robotic platform. Traditional sensing modalities such as visual cameras and Light Detection and Ranging (LiDAR) fail in environments with poor visibility due to darkness, smoke, or reflective surfaces. In these visioned-impaired conditions, UWB radar offers a promising alternative. To this end, this work explores the suitability of robot-mounted UWB radar for environmental mapping in dynamic, anchor-free scenarios. The study investigates how different materials (metal, concrete and plywood) and UWB radio channels (5 and 9) influence the Channel Impulse Response (CIR). Furthermore, a processing pipeline is proposed to achieve reliable mapping of detected obstacles, consisting of 3 steps: (i) target identification (based on CIR peak detection), (ii) filtering (based on peak properties, signal-to-noise score, and phase-difference of arrival), and (iii) clustering (based on distance estimation and angle-of-arrival estimation). The proposed approach successfully reduces noise and multipath effects, resulting in an obstacle detection precision of at least 82.36% and a recall of 89.46% on channel 9 even when detecting low-reflective materials such as plywood. This work offers a foundation for further development of UWB-based localisation and mapping (SLAM) systems that do not rely on visual features and, unlike conventional UWB localisation systems, do not require on fixed anchor nodes for triangulation.

INDEX TERMS Autonomous Navigation, Environment Mapping, Obstacle Detection, Radar, SLAM, Ultra-wideband (UWB)

I. INTRODUCTION

THE ability to detect objects and build a representation of the surrounding environment is an essential requirement to allow autonomous operations of mobile robots. Existing systems rely on cameras to capture images and track movement by extracting visual features. However, this method depends on clear lighting conditions and struggles in environments with low visibility, shadows, or reflective surfaces [11]. Light Detection and Ranging (LiDAR) systems, on the other hand, use laser pulses to measure distances and construct maps. While highly accurate, LiDAR sensors face challenges in environments where laser beams are scattered or absorbed, such as in heavy rain, fog, or areas with multiple reflective surfaces. Given these challenges, there is a growing need for alternative localisation and mapping technologies. Ultra-wideband (UWB) is a promising alternative due to its ability to operate in low-visibility environments while maintaining high accuracy (typically under 20 cm). However, UWB-based localisation systems usually rely on anchor-tag setups, where

fixed UWB anchors are installed in predefined locations, and mobile robots are equipped with UWB-tags [15] [19]. Although this setup works well for environments with stable infrastructure, it is impractical in dynamic or unknown places, such as search and rescue activities or industrial facilities where the surroundings frequently change. Furthermore, using a UWB radio instead of LiDAR can reduce the system's total weight, a significant advantage for drones that need to be as lightweight as possible to maximize autonomy [13].

To realize this vision, this paper proposes and evaluates signal processing methods to detect obstacles and map the environment using UWB radar systems mounted on mobile robots. The main contributions of this paper are as follows:

- We analyse how three common obstacle materials (metal, concrete, and plywood) affect the Channel Impulse Response (CIR), and identify optimal signal parameters (peak width and prominence) for obstacle detection of these materials across IEEE 802.15.4 UWB channels 5 and 9.

- We propose a novel noise filtering method that eliminates multipath-induced phantom reflections by computing a reliability score based on peak characteristics, signal-to-noise ratio (SNR) and phase-difference of arrival (PDoA).
- We broaden the radar's field of view by clustering detected reflections using combined distance and angle-of-arrival (AoA) estimations, enabling spatially coherent obstacle mapping.
- We evaluate the complete processing pipeline in realistic conditions within a large industrial testbed environment.
- We publicly release the captured dataset, processing pipeline, and an illustrative video to support reproducibility and further research¹.

The remainder of this paper is organised as follows: Section II provides background information on UWB. Section III discusses related work, whereas Section IV presents the proposed processing pipeline. In Section V, the data collection is explained, and the results for the proposed method are presented in Section VI together with a visual demonstration. Finally, Sections VII and VIII cover suggestions for future work and the conclusion, respectively.

II. BACKGROUND OF ULTRA-WIDEBAND

UWB is a radio technology that transmits data over a wide frequency range, either with an absolute bandwidth greater than 500 MHz or a fractional bandwidth (B_F) greater than 20%. The fractional bandwidth (B_F) is defined as the ratio of the signal's bandwidth (B_W) to its centre frequency (f_C). The fractional bandwidth (B_F) is defined as:

$$B_F = \frac{BW}{f_C} = \frac{(f_H - f_L)}{(f_H + f_L)/2}$$

Where f_H and f_L are the upper and lower frequencies of the -10 dB bandwidth [8].

Because UWB technology uses a large bandwidth, it enables the transmission of extremely short, narrow pulses in the time domain as described by the time-bandwidth relation $BW \times T \geq \frac{4}{\pi}$, where (B_W) is the signal's bandwidth and (T) the pulse duration. For example, UWB systems using a 500 MHz bandwidth can generate pulses of only 0.16 ns wide, whereas traditional technologies such as Wi-Fi, which are limited to bandwidths around 20 MHz, produce pulses longer than 4 ns. Due to its high bandwidth and ultra-narrow pulses, UWB is considered to have a high range resolution and ability to distinguish multiple targets [8].

This technology operates within the frequency spectrum of 3.1 GHz to 10.6 GHz, enabling data transmission speeds of up to 110 Mbps, typically with a range of up to 10 meters. A higher range of up to 100 meters is also possible, but at lower data rates, depending on several factors, including channel frequency, antenna design, power levels, and complexity of the propagation environment [17].

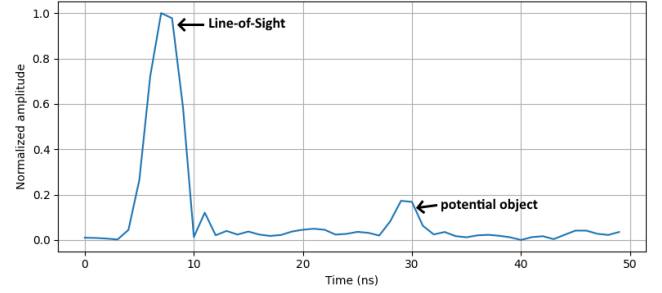


FIGURE 1. Example of a Channel Impulse Response where the object is placed at a distance of 3.5 m.

To better understand how UWB radar performs in realistic environments, it is essential to study how the transmitted signal interacts with obstacles and reflections in the environment. This is described by the Channel Impulse Response (CIR), illustrated in Fig. 1. The first peak in the figure corresponds to the Line-of-Sight (LoS) component, which is the earliest signal arriving directly from the transmitter to the receiver assuming no obstacles in between. In this case, the LoS signal indicates the signal transmitted from the transmitter antenna to the receiver antenna co-located on the same robot. The antennas are separated by a distance of 21 cm. Subsequent peaks represent reflections from other objects, walls, or multipath components.

The CIR is typically modelled as a sum of deterministic and diffuse multipath components [9] and it is expressed as shown in (1):

$$CIR(t) = \sum_i a_i \delta(t - \tau_i) + n_i \quad (1)$$

where the receiving pulse i has an amplitude a_i , time delay τ_i and noise n_i . In UWB radar systems, the CIR data is typically obtained as I/Q samples (In-Phase and Quadrature components) of the received signal, which provides important information about the signal's strength and phase.

UWB radar is widely used in applications that require precise distance measurements, even in cluttered or dynamic environments. Some examples of these applications are presence detection, device-free localisation, monitoring vital signs without physical contact and, activity recognition [8]. UWB is a strong candidate for fast-moving robots and dynamic environments due to its low weight, low power consumption, and cost-effectiveness [13]. While RGB cameras are also lightweight and energy-efficient, they suffer in complex or low-light environments. LiDAR offers high-accuracy long-range sensing but is heavy, power-intensive, and less effective in fog or smoke. Vanhie-Van Gerwen et al. [7] show that across various drone sizes, UWB stands out for its favourable accuracy-to-cost ratio. It also provides precise positioning thanks to its wide bandwidth and short pulses, is resistant to narrowband interference, and respects privacy by not capturing identity-related data.

¹Link to be released upon acceptance.

TABLE 1. Overview of Related Work in UWB-Based Object Detection and Distance Estimation

| Paper | Goal | Approach | Chip | UWB Mobile robot | No Anchor-Tags | Distance Estimation | Angle Estimation of Objects | IEEE 802.15.4 Compliant | Target Object | Detection Accuracy |
|------------|---|--|----------------------------------|------------------|----------------|---------------------|-----------------------------|-------------------------|---|--|
| [9] | Object/person detection using CIR analysis | Three CIR processing techniques (ICIR, UCIR, ACIR) with BMA and BSDA algorithms | DW1000 | - | ✓ | ✓ | - | ✓ | whiteboard, large tv, metal box, person | Avg. error ≤ 9 cm using ACIR (larger for persons or smaller objects) |
| [2] | Detect humans/obstacles in automatic train pairing. | Supervised Machine Learning | P440 from TimeDomain | - | ✓ | - | - | - | humans/obstacles | Best detection accuracy: 55%-70% indoors, > 95% outdoors |
| [16] | Remove clutter to improve detection accuracy | Low-rank approximation and singular value decomposition methods | not specified | - | ✓ | ✓ | - | - | walking person | Avg. error < 20 cm, RMSE < 50 cm |
| [1] | Distinguish objects from noise in transportation use cases. | Uses Discrete Wavelet Transform to extract features and forward these to the LSTM network. | UMAIN HST-D3 directional antenna | - | ✓ | - | - | - | pedestrian, cyclist, vehicle, tram | 72.78% precision, 71.34% recall, 72.06% F1-score |
| [3] | Detect the target object | Utilises signal's entropy | UMAIN HST-D3 directional antenna | - | ✓ | - | - | - | pedestrian, cyclist, vehicle, tram | 75.34% precision, 63.06% recall, 68.65% F1-score |
| [21] | UWB SLAM | wheel odometry and Extended Kalman Filter | X4M300 | ✓ | ✓ | ✓ | - | - | vertical metal rods | 6.2 cm localisation error |
| [22] | UWB SLAM in feature-deficient areas | Extends previous approach with UWB AoA anchor-tag for better loop closure | X4M300 | ✓ | - | ✓ | - | - | vertical metal rods | 10.3 cm localisation error |
| This paper | Reduce noise and unwanted multipath for reliable obstacle mapping | Filtering on peak properties, SNR-score, PDoA and clustering | QM33120W [5] | ✓ | ✓ | ✓ | ✓ | ✓ | metal plate, concrete and plywood box | Avg. error ≤ 8.50 cm, precision $\geq 82.36\%$, $\geq 89.56\%$ recall on channel 9 |

III. RELATED WORK

UWB is widely known for its use in localisation and anchor-tag positioning, where fixed UWB infrastructure ('UWB anchor nodes') is used to localise mobile robots. Although highly accurate, these localisation approaches require significant infrastructure investments and are hence outside the scope of this paper. Instead, in this section, we discuss prior works that focused on obstacle detection using fixed or mobile UWB radar systems and compare how they differ from our work.

Table 1 shows a comparison of the existing work with our approach. Most state-of-the-art solutions rely on the installation of fixed UWB radar systems. For example, Van Herbruggen et al. [9] introduce Accumulation Channel Impulse Response (ACIR) technique, which improves signal resolution for obstacle detection. Although this method increases the detection accuracy, it requires the collection of sufficient background data before it can be applied, and is therefore not suitable for dynamic environments with a moving robot as background collection can only be done in static environments where data can be collected before obstacles are present. Moreover, their ACIR approach requires collecting multiple CIR samples per measurement, limiting the maximum speed of robotic platforms with UWB radar. From the research of Sattiraju et al. [2] it is concluded that Random Forest and Extra Trees have the highest accuracy in obstacle detection. However, these methods are prone to overfitting the training data, which makes the model generalise less in

new environments. Yun et al. [16] suppress noise from the received signal using singular value decomposition (SVD). Although their method achieves high accuracy, the required matrix computations are computationally intensive and may increase the latency and memory usage for real-time mobile robots. Mimouna et al. [1], [3] focus on obstacle detection, but lack characterisation of the obstacle (e.g. estimation of distance and width). Moreover, the use of complex deep learning models in [1] would lead to a higher execution time. The method presented in this work overcomes all the above limitations by using clustering that is more adaptable to unseen and dynamic environments. Moreover, our work also characterizes the position and width of detected obstacles by combining both distance estimation and AoA information.

To the best of our knowledge, only two publications focus on robot-mounted UWB radar systems [21] and [22], but they both focus more on SLAM localisation aspects than UWB signal processing optimisations for obstacle characterisation. They are also limited by recognizing only vertical rods rather than reconstructing full obstacle representations from various material types. The proposed approach from our work can serve as a complementary method to [21] and [22], aiming to suppress noise and mitigate ghost detections while increasing the overall performance of their proposed UWB-SLAM algorithm. Unlike [22], which complements UWB SLAM with localisation by employing AoA nodes for robot localisation and loop closure, our paper focuses on estimating the AoA of detected objects using the PDoA between antennas on the

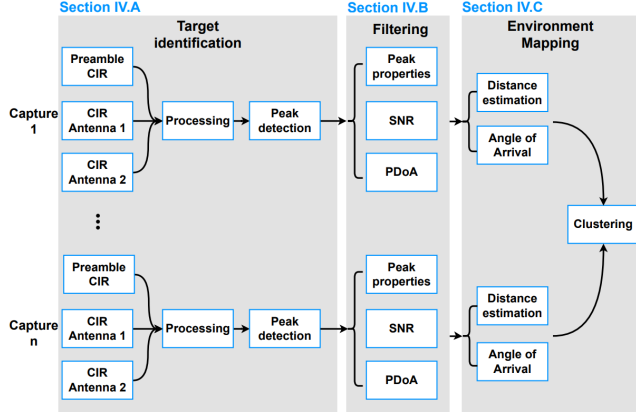


FIGURE 2. Overview of the proposed approach: Each captured row contains the preamble CIR and two additional CIRs from both antennas on the same chip used for calculating the PDoA. These are processed independently followed by filtering out noise or unwanted multipath components using peak properties, SNR-score, and PDoA. The distance to the object is estimated and the AoA is then calculated. Subsequently, multiple rows are combined to cluster reflections from the same object and map the environment.

same chip.

Finally, almost all prior work relies on custom UWB radar-only hardware devices with larger bandwidths and thus higher range resolution. Instead, our proposed approach is fully compliant with low-cost IEEE 802.15.4 standard off-the-shelf hardware, meaning the UWB radar system on our robot is low-cost, and the same hardware could also be used for localisation and communication in case fixed infrastructure would be available, thereby enabling low-cost joint sensing, communication and localisation for robotic platforms [18].

IV. PROPOSED APPROACH

This section outlines the complete workflow of the proposed approach for environment mapping. As illustrated in Fig. 2, it consists of three main steps: (i) target identification, (ii) signal filtering, and (iii) the combination of the individual observations for obstacle and environment mapping.

A. STEP 1: TARGET IDENTIFICATION

UWB offers high time resolution due to its large bandwidth and narrow pulses. This enables the precise differentiation in time of multiple reflected signals. An illustration of this effect is provided in Fig. 3, which shows the CIRs measured for metal, concrete, and plywood obstacles, overlaid on a background CIR measured without any obstacles. The reflections caused by each material appear as distinct peaks at specific delays relative to the first path.

The UWB receiver creates three types of CIRs: a preamble CIR, and two CIRs obtained from the Scrambled Timestamp Sequence (STS), received respectively on the first and second antenna integrated on the same chip. The preamble CIR is used for distance estimation, while the two STS-based CIRs are used to estimate the PDoA between the antennas. Because the same signal reaches each antenna with slightly differ-

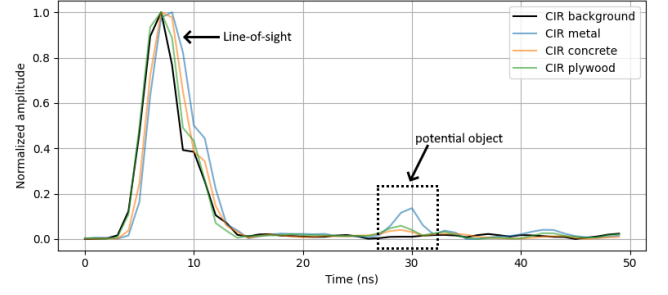


FIGURE 3. The CIRs measured for metal, concrete and plywood objects, overlaid on a background CIR measured without any obstacles. The reflections caused by each material appear as distinct peaks at specific delays relative to the first path. The metal object (blue) is clearly visible compared to the background.

ent phase, comparing these CIRs allows for angle of arrival (AoA) estimation.

1) Signal processing

To reliably extract the peak indicating an object, every raw CIR undergoes the following processing phases. Firstly, the CIR samples are initially recorded as complex values consisting of in-phase (I) and quadrature (Q) components. To calculate the amplitude of the received signals, Formula (2) is used on the Preamble CIR and Formula (3) is used to calculate the phase of the received signals on both STS-based CIRs.

$$CIR_{amplitude} = \sqrt{I^2 + Q^2} \quad (2)$$

$$\phi = \arctan\left(\frac{Q}{I}\right) \quad (3)$$

The first four samples of the CIRs are excluded from further processing, as these samples precede the arrival of the first signal and represent the noise floor. However, these initial samples are used later for calculating the Signal-to-Noise-Ratio (SNR) for filtering purposes. At last, to ensure a consistent threshold and comparability across different measurements, the preamble CIR is normalized using min-max scaling.

2) Peak detection

Peak detection is performed on the preamble CIR by identifying local maxima through comparison with neighbouring values. Subsequently, peaks are filtered based on their properties, as illustrated in the following step.

B. STEP 2: FILTERING

The filtering phase is applied to remove peaks that are likely to correspond to noise or unwanted multipath effects. This filtering process is based on four criteria:

- *width*: the minimum required width of a peak to be considered significant. Narrow peaks are more likely to represent noise, whereas reflections from physical objects typically produce broader peaks.

TABLE 2. Mathematical symbols used throughout this paper

| Variable | Description | Unit |
|-------------------|--|---------------------------------|
| B_F | Fractional bandwidth | - |
| B_W | Signal's bandwidth | Hz |
| F_C | Centre frequency | Hz |
| F_H and F_L | Upper and lower frequency of the -10 dB bandwidth | Hz |
| $CIR(t)$ | Channel Impulse Response | - |
| $CIR_{amplitude}$ | Amplitude of an I/Q sample | - |
| ϕ | Phase of an I/Q sample | radians |
| $SNR-score_i$ | SNR-based score for peak with index i | - |
| A_i | Amplitude of peak with index i in the CIR | - |
| A_{noise} | The RMS of noise floor in the CIR | - |
| k | Linear weighting factor for calculating the SNR-score | - |
| $d_{obstacle}$ | Distance between transmitter and object | cm |
| ToF | Time of Flight | ns |
| c | Speed of light | $(3.0 \times 10^8 \text{ m/s})$ |
| d_{TX-RX} | Average distance between the transmitter and four receivers | cm |
| α | Phase difference between the two antennas on the same chip | radians |
| θ | Angle of arrival | radians |
| TP | True positive, the reflection that indicates a real object | - |
| FP | False positive, the reflection that indicates a real object, but is actually noise | - |
| FN | False negative, the reflection that indicates a real object, but is filtered out | - |
| P | Precision calculated as $TP / (TP + FP)$ | - |
| R | Recall calculated as $TP / (TP + FN)$ | - |
| $F1-score$ | Calculated as $2 \times (P \times R) / (P + R)$ | - |

- *prominence*: represents how much a peak stands out due to its height and its location relative to other peaks, and is defined as the amplitude between the peak and its lowest contour line.
- $SNR-score_i$: the minimum required SNR-score for a detected peak to be considered a real object. The score is calculated as shown in (4).

$$SNR-score_i = 20 \log_{10} \left(\frac{A_i}{A_{noise}} \right) + k \times delay_i \quad (4)$$

Where A_i is the amplitude of the detected peak (at index i) and A_{noise} is calculated as the root mean square (RMS) of the noise floor. Additionally, to account for signal loss caused by the distance, a linear weighting is applied to the score based on a weighting factor k (0.20 in this case) and time delay $delay_i$ between the peak index and the first path index. This adjustment helps detect objects farther away as they naturally have a lower signal amplitude.

- *PDoA*: The antenna array's sensitivity and resolution degrade at wider angles, leading to increased multipath interference and reduced angular accuracy. As such, peaks corresponding to reflections from angles outside the range of -45° to 45° are discarded, as estimates beyond this interval are considered unreliable.

The exact values of the filtering parameters and how they impact accuracy will be discussed in Section VI-A.

C. STEP 3: ENVIRONMENT MAPPING

The final stage of the proposed method combines the processed observations into a representation of the environment. This process involves three iterative steps: distance estimation, AoA determination and clustering. The distance estimation provides the range of each reflection, whereas the AoA is used to position the detected objects relative to the robot. Finally, reflections originating from the same location are grouped through clustering.

1) Distance Estimation

For obstacle detection, the peak with the highest amplitude (excluding the first path) that meets all the conditions is selected, as it is most likely to correspond to a real object. This is illustrated in Fig. 3. Each peak beyond the first path arrives later because the reflected signal travels a longer time than the direct path. Therefore, the Time-of-Flight (ToF) of the reflected signal is used to estimate the distance to the object as illustrated in (5).

$$d_{obstacle} = \sqrt{\left(\frac{(ToF \times c) + d_{TX-RX}}{2} \right)^2 - \left(\frac{d_{TX-RX}}{2} \right)^2} \quad (5)$$

Where:

- ToF is the time delay in seconds,
- c is the speed of light ($3 \times 10^8 \text{ m/s}$),
- d_{TX-RX} is the average distance between the transmitter (TX) and each receiver (RX) (21 cm in this case),

This equation accounts for the fact that the transmitter and receiver are physically separated by a fixed distance d_{TX-RX} and calculates the perpendicular distance from the transmitter, which is positioned in the middle of the mobile robot, to the object.

2) Angle of Arrival

Once the distance to the obstacle is known, the relative position of the obstacle is calculated. To estimate the AoA, the PDoA between the two antennas on the same chip is used, following the methods of Dotlic et al. [14]. The PDoA, shown in Formula (6), and adapted from [14], no longer requires synchronization since both antennas are on the same chip. Next, in Formula (7), the AoA is calculated using the PDoA.

$$\alpha = ((-\phi_A + \phi_B + \pi) \bmod 2\pi) - \pi \quad (6)$$

Here ϕ_A and ϕ_B are the phases measured at antenna A and B.

$$\theta = \frac{1}{0.95} \cdot \arcsin\left(\frac{\alpha}{\pi}\right) \quad (7)$$

Tests show that the estimated AoA generally follows the ground truth when the object is in front of the robot. Some deviations appear, especially when approaching the object from the side, but these estimates remain useful for filtering.

3) Clustering

By applying the filtering methods from step 2, and localising the resulting points relative to the robot using the distance and orientation calculations, a point cloud of potential obstacle reflections is generated. In this final step, a clustering algorithm then removes outliers and groups these points into likely obstacle regions. To this end, the *Density-Based Spatial Clustering of Applications with Noise (DBSCAN)* is used.

DBSCAN is well suited for this work because reflections from real objects tend to appear repeatedly in the same location, forming dense groups of points. By identifying these dense regions, DBSCAN can cluster reflections that originate from the same physical object while simultaneously discarding isolated points as noise.

The most important parameter for DBSCAN in this work is *epsilon (eps)*, which defines the maximum distance between two samples for one to be considered in the neighbourhood of the other. The second key parameter is *min_samples* which is the number of samples in a neighbourhood for a point to be considered as a core point, including the point itself. Clusters smaller than these thresholds are discarded as noise. In this paper, *eps* was set to 20 cm and *min_samples* to 20 reflections. Choosing a smaller value would reduce the number of points labelled as noise, but at the risk of forming incorrect clusters that do not correspond to real objects, which would in turn degrade mapping accuracy.

V. DATA COLLECTION

The following data collection experiments were conducted to evaluate the effectiveness of the proposed approach and assess its performance under realistic conditions. The data collection experiments were conducted in the controlled Industrial Internet of Things (IIoT) lab at Ghent University [4] focusing on object detection and signal behaviour using UWB radar. All experiments were performed using a TurtleBot 4 robot, equipped with one omnidirectional UWB transmitter on the top and four dual-antenna, directional UWB receivers on every side (Fig. 4a). To reduce the impact caused by the first path signal as the transmitter is placed close to the receiver, an absorber is used (Fig. 4b). The specifications of the radar system are listed in Table 3. During data capture, the system alternated between channel 5 and channel 9 for each measurement to assess signal behaviour across different frequency bands. The IIoT lab is equipped with a Motion Capture (MOCAP) system, providing millimetre-level accuracy ground truth data as the robot moves.

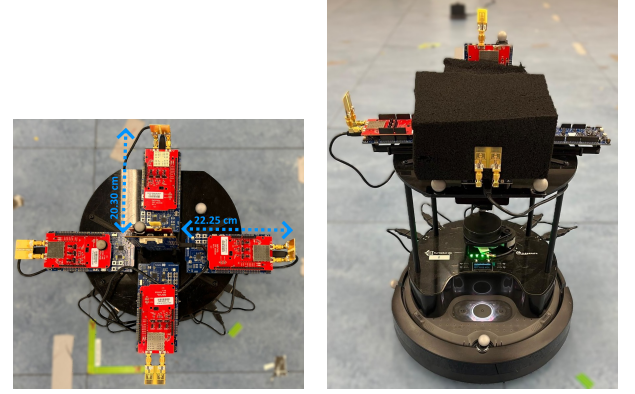


FIGURE 4. a) Overview of the antenna placement on the TurtleBot 4 including the distance between the transmitter and receivers. b) Front view of the TurtleBot 4, equipped with the antennas and absorber.

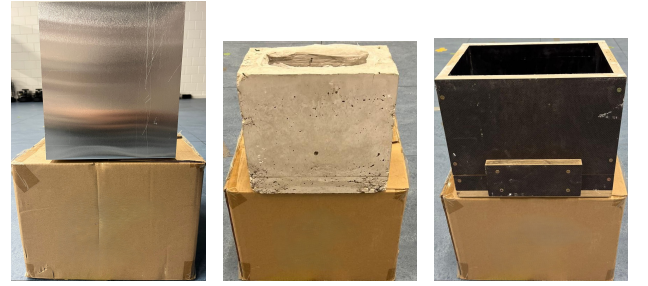


FIGURE 5. a) metal plate measuring 25 cm x 28 cm b) concrete box measuring 28 cm x 24 cm c) plywood box measuring 31.5 cm x 26 cm

A. FIRST DATA COLLECTION: DIFFERENT MATERIALS

The goal of this data collection was to analyse how UWB radar signals behave depending on the type of material. Three different objects were used in the experiments: a metal plate measuring 25 cm x 28 cm (Fig. 5a), a concrete box measuring 28 cm x 24 cm (Fig. 5b), and a plywood box measuring 31.5 cm x 26 cm (Fig. 5c). These materials were selected for their varying electromagnetic properties: the metal plate is highly reflective, the concrete box partially reflects and absorbs signals, and the plywood box primarily absorbs with minimal reflection. As shown in Fig. 6a, the robot moved in a

TABLE 3. UWB Radar Specifications - IEEE 802.15.4 compliant

| Parameter | Value |
|---------------------------|--------------------------------------|
| UWB sensor | QM33120W [5] |
| Preamble length | 512 |
| Frequency | 6.5 GHz and 8 GHz |
| Channel | 5 and 9 |
| Bandwidth | 500 MHz |
| Transmitter specification | JL159 Omnidirectional single antenna |
| Receiver specification | JL359 Directional dual antenna |
| Update rate | 96 Hz |
| Number of I/Q samples | 50 I/Q pairs |

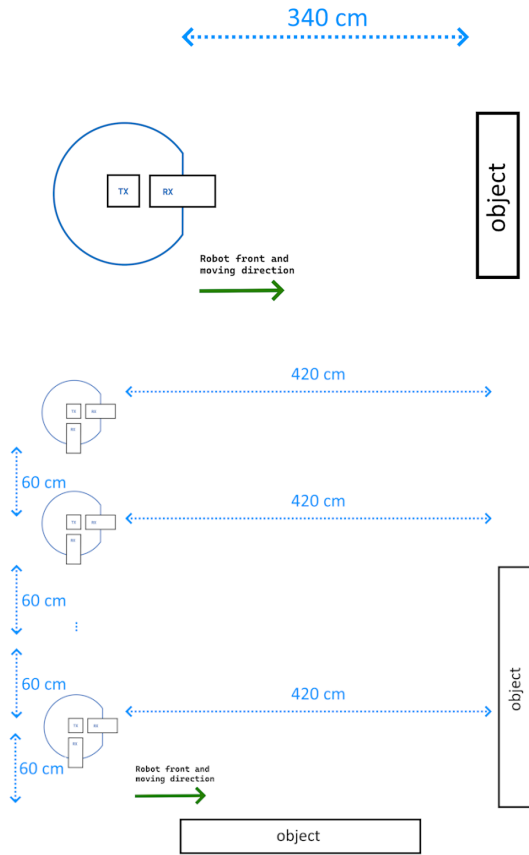


FIGURE 6. a) First data collection: the robot moves straight forward to the object. The same movement is done three times, once for every material (metal, concrete, plywood). b) Second data collection: two objects are placed, in the front and parallel to the robot while data is captured using two receivers.

straight line toward a single object, starting from a distance of 340 cm. For this experiment, only the top transmitter and front receiver were active. Due to the use of different materials, this setup is a good validation of the accuracy of recognizing different material types.

B. SECOND DATA COLLECTION: MULTIPLE OBJECTS

The second data collection aimed to explore the ability to detect reflections from objects not placed directly in front of the receiver. In this setup, two white plates made of highly reflective material with dimensions of 116 cm by 55 cm were placed as target objects, one directly in front of the robot and the other parallel to its path to test if the front antenna could detect signals from the side or vice versa (Fig. 6b). The robot started from a distance of 420 cm from the front plate and 60 cm from the parallel plate. The distance to the parallel object increased in 60 cm steps up to 300 cm, while the robot was repositioned at the same start point. Since both objects are highly reflective, this setup creates many multipath components and phantom peaks and is hence a good validation of the efficiency of the filtering algorithm.

VI. RESULTS

This section presents and analyses the results from the proposed processing pipeline. It begins with an overview of the filtering parameters, followed by an analysis of target identification, filtering performance and clustering behaviour. This section concludes with a visual demonstration to validate all subcomponents.

The performance of the proposed approach is evaluated using two types of metrics: (i) detection probability and (ii) distance accuracy (expressed as distance error to indicate how well obstacles are positioned relative to the robot). Detection probability is expressed as Precision P , Recall R , and F1-score, as defined in Formulas (8)-(10):

$$P = \frac{TP}{TP + FP} \quad (8)$$

$$R = \frac{TP}{TP + FN} \quad (9)$$

$$F1\text{-score} = 2 \times \frac{P \times R}{P + R} \quad (10)$$

Where TP (true positives) are reflections correctly retained that correspond to actual objects, FP (false positives) are retained reflections that do not correspond to real objects (e.g. walls or noise), and FN (false negatives) are reflections incorrectly removed that do correspond to actual objects. For detection probability, a margin of 20 cm is used when comparing estimated distances to ground truth: an estimated reflection is considered a true positive if it lies within 20 cm of the ground truth object.

A. FILTERING PARAMETERS

The three key parameters (peak *width*, *prominence*, and *SNR-score*) were optimised using the dataset obtained from the first data collection (Fig. 6a). A grid search over different parameter values was performed, and each configuration was evaluated using the $F1\text{-score}$ and the root mean squared error (RMSE) between the estimated and ground-truth distances. The parameters achieving the highest $F1\text{-score}$ and lowest RMSE were selected. To further investigate their behaviour, the relationship between distance and both peak prominence and width was analysed for the three different materials (metal, concrete, plywood). Figures 7a and 7b illustrate the correlations in peak prominence and width as a function of target distance.

As seen in Fig. 7a, peak prominence decreases as the distance increases. At short ranges, the reflected signals retain more energy and produce stronger peaks. With increasing distance, signal attenuation and energy loss cause the peaks to stand out less compared to other peaks or the noise floor. Metal consistently produces the highest peak prominence, which is expected given its high reflectivity. Concrete and plywood, by comparison, show lower prominence because they absorb more energy and reflect less. At the shortest distances, concrete can not be detected as the peak prominence

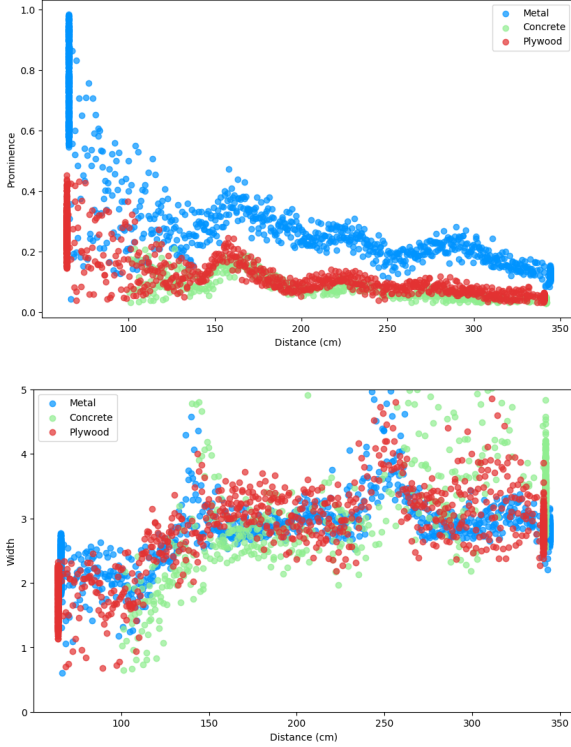


FIGURE 7. Correlation between peak properties and distance: a) Prominence decreases with distance for all materials. b) Width increases as the distance increases for all materials.

and width are too low. As distance grows, both concrete and plywood follow a similar downward trend.

Fig. 7b shows that the peak width increases with distance for all three materials. Close to the robot, the peaks are relatively narrow (around 1-2 ns), but at greater distances they broaden to approximately 3-4 ns. This broadening occurs because, over longer distances, the UWB signal spreads out and undergoes more reflections and scattering. The time delay makes the signal arrive over a longer period, which appears as a broader peak in the CIR.

Finally, width, prominence, and SNR-score were tuned using the *F1-score*, which balances precision and recall. The optimised values are summarised in Table 4, both for specific materials and overall optimal values across different materials. The remainder of this section uses the overall filtering parameters listed in Table 4. These parameters represent the best configuration for mixed-material environments containing metal, concrete, and plywood. If the material in the environment is known beforehand (i.e., only one material type is present), parameters specific to that material type can be used to further improve detection performance.

B. TARGET IDENTIFICATION, FILTERING, AND MAPPING ACCURACY

1) Impact of different materials

The performance of the algorithm differed clearly across materials and channels, the detection accuracy results are shown

TABLE 4. Optimal peak width, peak prominence and SNR-score values for different materials and multiple radio channels.

| Channel | Material | Width | Prominence | SNR-score |
|---------|----------|-------|------------|-----------|
| 5 | Metal | 1 | 0.04 | 25 |
| | Concrete | 1 | 0.05 | 20 |
| | Plywood | 1 | 0.02 | 15 |
| | Overall | 1 | 0.05 | 20 |
| 9 | Metal | 1 | 0.05 | 20 |
| | Concrete | 2 | 0.03 | 10 |
| | Plywood | 0.10 | 0.01 | 10 |
| | Overall | 0.20 | 0.03 | 10 |

in Table 5 and the detection probability in Fig. 8.

Metal: Both channels detected the metallic plate with very high accuracy. On channel 5, the mean error was 7.18 cm with precision and recall above 93%. Channel 9 further improved accuracy, reducing the mean error to 5.93 cm and achieving nearly perfect precision and recall.

Concrete: Detection was more challenging for the concrete box. On channel 5, the object was only detected starting at 250 cm, with higher variability (mean error 19.16 cm, SD 37.29 cm) and reduced precision (78.41%). Recall remained high (95.17%), but the large number of outliers increased the error. At close range (<100 cm), the signal was overshadowed by the first path and the object was not detected on both channels 5 and 9. In contrast, channel 9 considerably improved performance: detection began at 340 cm, mean error dropped to 10.84 cm, and precision increased to 82.36%. Fig. 7a and Fig. 7b illustrate that concrete is overshadowed at close distances because the width and prominence are relatively low.

Plywood: Results on channel 5 were the weakest, with low precision (69.50%) and moderate recall (74.45%). This is primarily due to the low amplitude of the reflection peak, which is often close to the noise floor and difficult to differentiate from background noise. More reliable detection occurred when the robot was within approximately 120 cm. Channel 9 improved performance noticeably: mean error decreased to 8.44 cm, and both precision (98.00%) and recall (99.23%) were near perfect, with consistent detection from 340 cm onward.

Overall, channel 9 consistently outperformed channel 5 for non-metallic materials, resulting in lower mean errors, fewer outliers, and higher precision/recall. Table 5 shows the higher variability of concrete and plywood in channel 5 compared to channel 9. In addition, further accuracy gains can be obtained during step 3 of the processing pipeline (see next sections).

2) Impact of combined filtering and clustering steps

The impact of each step of the complete processing pipeline is illustrated in Fig. 9. For this visualisation, data was collected using the parallel antenna in an environment with two objects (illustrated in Fig. 6b). Each sub-figure includes a colour bar on the right-hand side representing the SNR score. Table

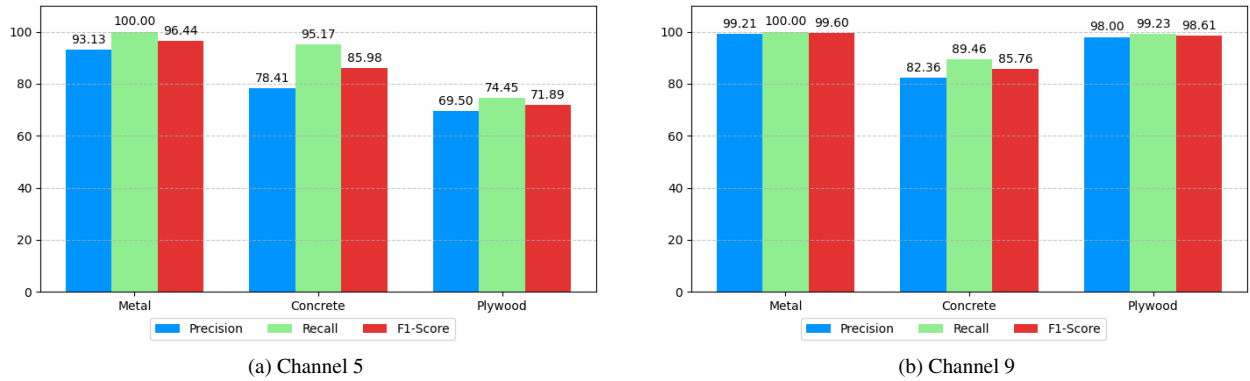


FIGURE 8. Detection performance metrics (precision, recall, F1-score) for each material and channel configuration. Metrics are based on correctly retained object reflections (true positives), noise reflections (false positives), and missed object reflections (false negatives).

TABLE 5. Obstacle detection accuracy (errors in cm) for different materials after step 2 (after filtering on width, prominence, snr-score, and PDoA)

| Channel | Material | Mean Accuracy | Standard Deviation | Median |
|---------|----------|---------------|--------------------|--------|
| 5 | Metal | 7.18 | 13.90 | 7.04 |
| | Concrete | 19.16 | 37.29 | 6.32 |
| | Plywood | 33.41 | 62.91 | 10.09 |
| 9 | Metal | 5.93 | 4.10 | 4.59 |
| | Concrete | 10.84 | 11.43 | 6.52 |
| | Plywood | 8.44 | 7.48 | 4.73 |

6 summarises the key parameters used in this work. These parameters may vary depending on the environment and the used channel; for instance, if the environment consists of a single material (e.g., metal, concrete, or plywood), parameters can be tuned accordingly. In this work, however, the overall parameters on channel 5 were used to ensure general applicability.

In the first step (Fig. 9a), all detected reflections are shown relative to the robot's location. Since object positioning will be implemented in the following steps, at this stage the calculated distances are simply added to the robot's location, assuming every reflection originates in front of its right antenna (x-axis). At this point, many unwanted reflections caused by noise and multipath effects are visible, which makes raw CIR unsuitable for direct mapping since it could easily lead to false object detections. To remove the unwanted reflections, the data is filtered in the next stage (Fig. 9b) using *width*, *prominence*, and *SNR-score* defined in Table 6. This step significantly reduces unwanted reflections and reveals a clear pattern. It also highlights an important behaviour of the parallel antenna: although it is mounted on the right side of the robot, it still detects reflections from objects that are not directly in front of it. In this example, reflections from an object located in front of the robot but outside the parallel antenna's forward-facing range are still recorded, resulting in

TABLE 6. Key parameters used in the proposed approach

| Parameter | Threshold | Comments |
|--------------------------|-------------------------|--|
| <i>width, prominence</i> | 1, 0.05 | Peak properties: minimum required width and prominence of a peak to be considered significant. |
| <i>SNR-score</i> | 20 | Reflections with a SNR-score lower than the threshold are discarded. |
| <i>AoA_range</i> | $[-45^\circ, 45^\circ]$ | Only reflections within this range are kept. |
| <i>eps</i> | 20 cm | DBSCAN parameter: max distance between two samples to be part of the same neighbourhood. |
| <i>min_samples</i> | 20 | DBSCAN parameter: number of samples in a neighbourhood for a point to be considered as a core point. |
| <i>min_reflections</i> | 50 | Minimum number of new reflections before clustering is applied. |
| <i>range</i> | 20 cm | Detected reflections within this range are classified as true positives. |
| <i>bias</i> | 20 cm | Calibration offset to correct systematic errors in distance measurements. |

a line of phantom reflections as shown in the figure diagonally down to the right.

To avoid such misleading detections, the following step (Fig. 9c) introduces filtering based on the PDoA. Only reflections with AoA between -45° - 45° are retained, since research has shown PDoA to be reliable within this range. Beyond these limits, phase wrapping can produce misleading estimates. Once this filtering is applied, the AoA is calculated from the phase difference (Fig. 9d) and the reflections are mapped relative to the robot's location, which in this case is tracked using the MOCAP system. The final step (Fig. 9e)

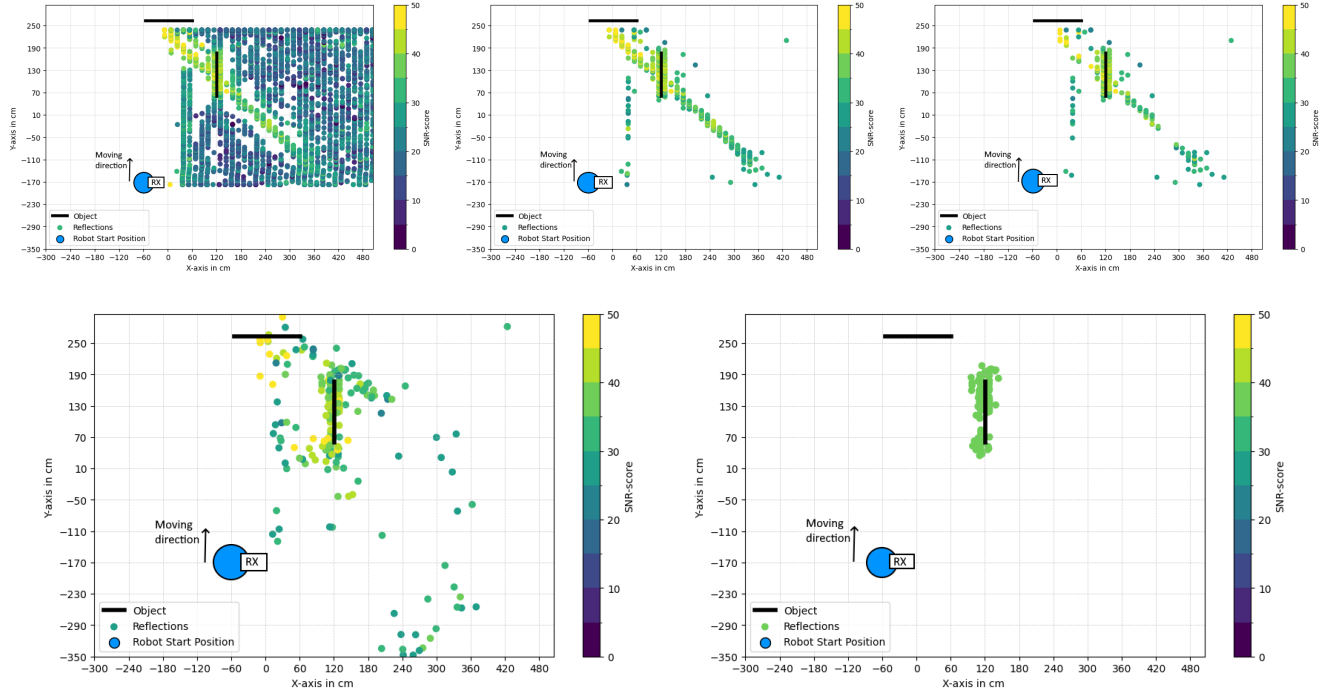


FIGURE 9. Overview of the impact of each of the multi-stage processing pipeline steps for object detection. For visual clarity, only the point cloud from the right-side antenna is shown. a) Peak detection: 5601 initial reflections b) Filtering on *width*, *prominence* and *SNR-score*: 444 remaining reflections c) Additional filtering on PDoA: 225 remaining reflections d) Calculating object position relative to the robot using AoA: 225 remaining reflections e) Proposed approach: Peak detection, filtering on peak properties, SNR-score, PDoA, calculating object position and clustering: 89 remaining reflections. The front object is not marked as this is outside the filtered $-45^\circ - 45^\circ$ field of view range of the side antenna.

applies clustering to the remaining reflections. Reflections that are close to each other are grouped into clusters, which likely represent real objects. The clustering is performed after more than *min_reflections* reflections have been recorded. Reflections that do not belong to any cluster are considered noise and discarded. As a result, the remaining clusters are assigned consistent SNR-based scores, which strengthens the confidence that they correspond to actual objects in the environment.

The accuracy of the end result of the overall processing pipeline is evaluated in Fig. 10, which presents the cumulative distribution function (CDF) of the errors compared to the ground truth. The results show a median error of 8.48 cm. Moreover, 90% of the errors are below 23.50 cm and 95% below 25.65 cm, demonstrating that the proposed method achieves high accuracy with low error rates.

3) Visual Demonstration of the Proposed Approach

From the experimental results, it can be concluded that channel 9 achieves the highest performances across all three tested material types. To provide a clearer understanding of this outcome, a visual demonstration is made available online². Fig. 11 illustrates the experimental setup, which consists of four obstacles (metal, concrete, and plywood), the mobile

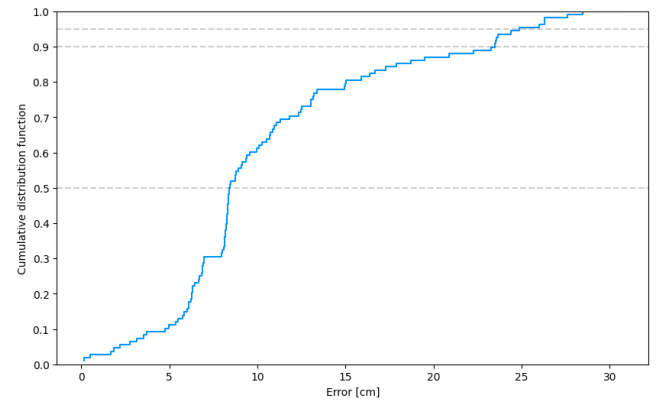


FIGURE 10. CDF illustrating the errors between the estimated object position and ground truth, 90% of the errors are below 23.50 cm and 95% below 25.65 cm.

robot, and its followed path. Fig. 12 presents the resulting environment map generated using our proposed approach.

VII. FUTURE WORK AND LIMITATIONS

This research identified two main limitations. First, when the robot approaches the object within approximately 60 cm, the object is no longer detected. This distance threshold was determined experimentally. At distances below 60 cm, the object's reflection peak becomes too close to the direct-path signal, causing it to be overshadowed. Additionally, multipath

²<https://www.youtube.com/watch?v=ci-uefoqRzY>

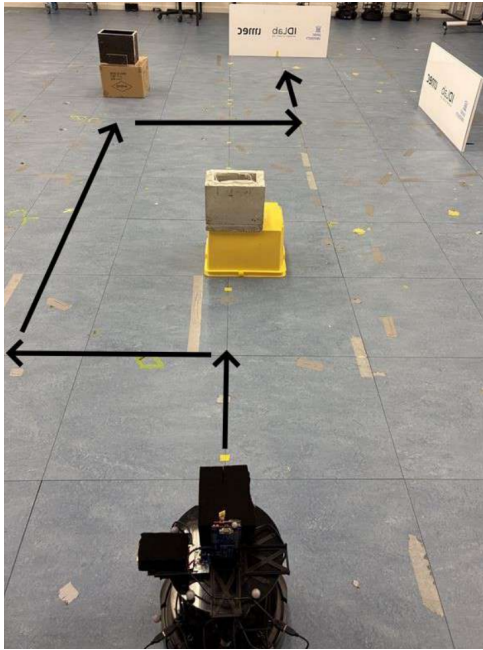


FIGURE 11. The lab setup containing four obstacles, the robot and its followed path.

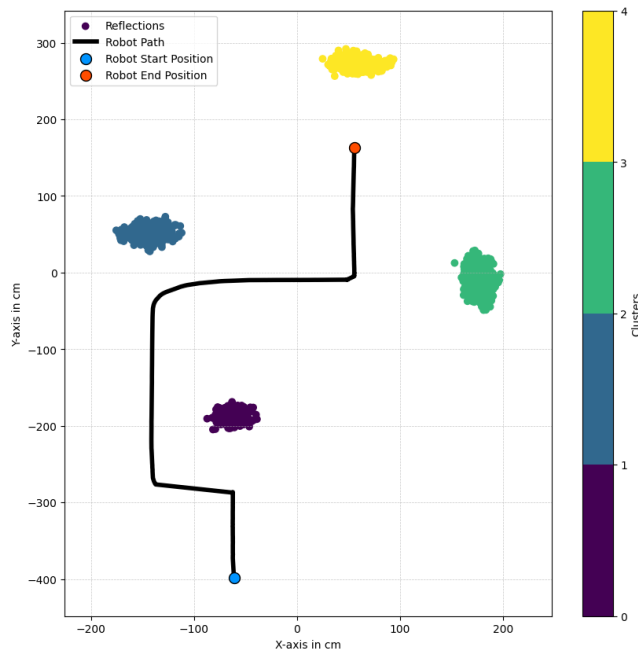


FIGURE 12. The resulting map showing the detected obstacles and their localisation using our proposed approach.

components generated by the direct signal may further complicate the separation of the object's peak. While this effect is primarily due to antenna design and the dominance of the direct path, the object's material properties also influence the outcome. Highly reflective materials generate stronger peaks, whereas absorptive materials produce weaker responses that are more easily masked. To ensure reliable detection at closer distances, improved antenna isolation between the transmitter and receiver could help reduce the direct-path signal, or higher bandwidth settings could be used to achieve better timing resolution. Second, the analysis showed that peak prominence decreases and width increases with distance; however, the filters used in this work employed fixed thresholds. In future work, adaptive thresholding methods could be implemented to account for distance-dependent variations in peak characteristics, thereby improving detection robustness across different ranges and reducing false positives and false negatives.

VIII. CONCLUSION

This paper presented an infrastructure-free UWB radar-based approach for obstacle mapping on mobile robots. The proposed method consists of three steps: (i) target identification (based on CIR peak detection), (ii) filtering (based on peak properties, signal-to-noise score, and phase-difference of arrival), and (iii) clustering (based on distance estimation and angle-of-arrival estimation). The experimental evaluation across channels 5 and 9 and three material types demonstrated that the proposed system achieved high distance-estimation accuracy and detection accuracy, with obstacle localisation errors below 11 cm and precision above 82% on channel 9. The filtering methods and clustering effectively suppressed noise and multipath reflections without requiring any prior background data, making it well suited for dynamic environments. By integrating AoA estimation, the approach enables object localisation and obstacle mapping, providing a strong foundation for use in SLAM and other real-time robotic applications.

REFERENCES

- [1] Amira Mimouna, Anouar Ben Khalifa, Ihsen Alouani, Abdelmalik Taleb-Ahmed, Atika Menhaj, and Najoua Essoukri Ben Amara. *LSTM-based System for Multiple Obstacle Detection using Ultra-wide Band Radar*. In: Proceedings of the 13th International Conference on Agents and Artificial Intelligence, 2021. DOI: 10.5220/0010386904180425.
- [2] Raja Sattiraju, Jacob Kochems, and Hans D. Schotten. *Machine learning based obstacle detection for Automatic Train Pairing*. In: 2017 IEEE 13th International Workshop on Factory Communication Systems (WFCS), pp. 1–4, 2017. DOI: 10.1109/WFCS.2017.7991962.
- [3] Amira Mimouna, Anouar Ben Khalifa, Ihsen Alouani, Najoua Essoukri Ben Amara, Atika Menhaj, and Abdelmalik Taleb-Ahmed. *Entropy-Based Ultra-Wide Band Radar Signals Segmentation for Multi Obstacle Detection*. IEEE Sensors Journal, vol. PP, 2021. DOI: 10.1109/JSEN.2021.3050054.
- [4] IDLAB Ghent University. Industrial IoT Lab resources. Available at: <https://idlab.ugent.be/resources/industrial-iot-lab>. Accessed: 2025-05-06.
- [5] Mouser – Qorvo QM33120WDK1 User Guide. *Qorvo QM33120WDK1 user guide*. Available at: https://www.mouser.be/datasheet/2/412/Qorvo_QM33120WDK1_UG_RevB-3075114.pdf. Accessed: 2025-05-07.

- [6] Clear Path Robotics – TurtleBot 4. *TurtleBot 4 – Robotics Learning Platform*. Available at: <https://clearpathrobotics.com/turtlebot-4/>. Accessed: 2025-05-27.
- [7] Jono Vanhie-Van Gerwen, Kurt Geebelen, Jia Wan, Wout Joseph, Jeroen Hoebeke, and Eli De Poorter. *Indoor Drone Positioning: Accuracy and Cost Trade-Off for Sensor Fusion*. IEEE Transactions on Vehicular Technology, vol. 71, no. 1, pp. 961–974, 2022. DOI: 10.1109/TVT.2021.3129917.
- [8] Mohammad Cheraghinia, Adnan Shahid, Stijn Luchie, Gert-Jan Gordebeke, Olivier Caytan, Jaron Fontaine, Ben Van Herbruggen, Sam Lemey, and Eli De Poorter. *A Comprehensive Overview on UWB Radar: Applications, Standards, Signal Processing Techniques, Datasets, Radio Chips, Trends and Future Research Directions*. IEEE Communications Surveys & Tutorials, 2024. DOI: 10.1109/COMST.2024.3488173.
- [9] Ben Van Herbruggen, Stijn Luchie, Rafael Berkvens, Jaron Fontaine, and Eli De Poorter. *Impact of CIR processing for UWB radar distance estimation with the DW1000 transceiver*. In: 2023 13th International Conference on Indoor Positioning and Indoor Navigation (IPIN), pp. 1–7, 2023. DOI: 10.1109/IPIN57070.2023.10332499.
- [10] Bashar Alsadik and Samer Karam. *The Simultaneous Localization and Mapping (SLAM) – An Overview*. Journal of Applied Science and Technology Trends, vol. 2, pp. 120–131, 2021. DOI: 10.38094/jastt204117.
- [11] Leyao Huang. *Review on LiDAR-based SLAM Techniques*. In: 2021 International Conference on Signal Processing and Machine Learning (CONF-SPML), pp. 163–168, 2021. DOI: 10.1109/CONF-SPML54095.2021.00040.
- [12] Misha Urooj Khan, Syed Azhar Ali Zaidi, Arslan Ishtiaq, Syeda Ume Rubab Bukhari, Sana Samer, and Ayesha Farman. *A Comparative Survey of LiDAR-SLAM and LiDAR based Sensor Technologies*. In: 2021 Mohammad Ali Jinnah University International Conference on Computing (MAJICC), pp. 1–8, 2021. DOI: 10.1109/MAJICC53071.2021.9526266.
- [13] Siyuan Chen, Dong Yin, and Yifeng Niu. *A Survey of Robot Swarms' Relative Localization Method*. Sensors, vol. 22, p. 4424, 2022. DOI: 10.3390/s22124424.
- [14] Igor Dotlic, Andrew Connell, Hang Ma, Jeff Clancy, and Michael McLaughlin. *Angle of arrival estimation using decawave DW1000 integrated circuits*. In: 2017 14th Workshop on Positioning, Navigation and Communications (WPNC), pp. 1–6, 2017. DOI: 10.1109/WPNC.2017.8250079.
- [15] Che-Cheng Chang, Yee-Ming Ooi, Shih-Tung Tsui, Ting-Hui Chiang, and Ming-Han Tsai. *Utilizing Ensemble Learning to Improve the Distance Information for UWB Positioning*. Applied Sciences, vol. 12, no. 19, article 9614, 2022. DOI: 10.3390/app12199614.
- [16] Younguk Yun, Yohan Park, Byung Moo Lee, Byeongchun Hyun, and Youngok Kim. *Distance Estimation Scheme Exploiting IR-UWB Radar with Clutter Suppressing Algorithm in Indoor Environments*. Journal of Electrical Engineering & Technology, vol. 14, no. 4, pp. 1759–1769, 2019. DOI: 10.1007/s42835-019-00207-9.
- [17] Dieter Coppens, Adnan Shahid, Sam Lemey, Ben Van Herbruggen, Chris Marshall, and Eli De Poorter. *An Overview of UWB Standards and Organizations (IEEE 802.15.4, FiRa, Apple): Interoperability Aspects and Future Research Directions*. IEEE Access, vol. 10, pp. 70219–70241, 2022. DOI: 10.1109/ACCESS.2022.3187410.
- [18] Ben Van Herbruggen, Stijn Luchie, Jelle Jocqué, Ruben Wilssens, Sam Lemey, and Eli De Poorter. *WiP paper: UWB-based integrated sensing and communication (ISAC) for robotic applications*. In: EWSN 2024, 21st International Conference on Embedded Wireless Systems and Networks, Proceedings, Abu Dhabi, UAE, 2024. Available at: <https://ewsn.org/file-repository/ewsn2024/ewsn24-final136.pdf>.
- [19] Cheng Tu, Jiabin Zhang, Zhi Quan, and Yingqiang Ding. *UWB indoor localization method based on neural network multi-classification for NLOS distance correction*. Sensors and Actuators A: Physical, vol. 379, p. 115904, 2024. DOI: 10.1016/j.sna.2024.115904.
- [20] Alex Moschevikin, Eugene Tsvetkov, Anton Alekseev, and Axel Sikora. *Investigations on passive channel impulse response of ultra wide band signals for monitoring and safety applications*. In: 2016 3rd International Symposium on Wireless Systems within the Conferences on Intelligent Data Acquisition and Advanced Computing Systems (IDAACS-SWS), pp. 97–104, 2016. DOI: 10.1109/IDAACS-SWS.2016.7805795.
- [21] H. A. G. C. Premachandra, Ran Liu, Chau Yuen, and U-Xuan Tan. *UWB Radar SLAM: An Anchorless Approach in Vision Denied Indoor Environments*. IEEE Robotics and Automation Letters, vol. 8, no. 9, pp. 5299–5306, 2023. DOI: 10.1109/LRA.2023.3293354.
- [22] Charith Premachandra, Achala Athukorala, and U-Xuan Tan. *All-UWB SLAM Using UWB Radar and UWB AOA*. IEEE Robotics and Automation Letters, vol. 10, no. 8, pp. 8171–8178, 2025. DOI: 10.1109/LRA.2025.3583601.



ADELINA GIUREA received the M.Sc. degree in Information Engineering Technology from Ghent University, Belgium, in September 2025. She is currently pursuing the Ph.D. degree with the ID-Lab Research Group, focusing on Ultra-wideband and Bluetooth Low Energy.



IR. STIJN LUCHIE was born in Veurne in 1999. He received his M.Sc. degree in Computer Science Engineering from Ghent University, Belgium, in September 2022. Shortly thereafter, in October 2022, he started as a researcher with the Department of Information Technology (INTEC) at Ghent University in the IDLab research group. His primary area of scientific interest centres on ultra-wideband technology, with a specific focus on the self-calibration of anchor networks and the applications of UWB radar.



DR. IR. DIETER COPPENS received the master's degree in electrical engineering from Ghent University, Belgium, in 2021 and the Ph.D. degree with the IDLab Research Group in 2025. His research interests are wireless networking, indoor localization system based on Ultra-wideband technology and machine learning.



PROF. DR. IR. JEROEN HOEBEKE received the Masters degree in Engineering Computer Science from Ghent University in 2002. In 2007, he obtained a Ph.D. in Engineering Computer Science with his research on adaptive ad hoc routing and Virtual Private Ad Hoc Networks. Current, he is an associate professor in the Internet Technology and Data Science Lab of Ghent University and imec. He is conducting and coordinating research on wireless (IoT) connectivity, embedded communication stacks, deterministic wireless communication and wireless network management. He is author or co-author of more than 200 publications in international journals or conference proceedings.



PROF. DR. IR. ELI DE POORTER is currently a Professor with the IDLab Research Group, Ghent University, and imec. His team performs research on wireless communication technologies such as (indoor) localization solutions, wireless IoT solutions, and machine learning for wireless systems. He performs both fundamental and applied research. For his fundamental research, he is currently the coordinator of several research projects (SBO, FWO, and GOA). He has over 200 pub-

lications in international journals or in the proceedings of international conferences. For his applied research, he collaborates with industry partners to transfer research results to industrial applications, and to solve challenging industrial research problems.

...